This document is confidential and is proprietary to the American Chemical Society and its authors. Do not copy or disclose without written permission. If you have received this item in error, notify the sender and delete all copies.

Thermoplasmonic Effect of Surface Enhanced Infrared Absorption in Vertical Nanoantenna Arrays

Journal:	*The Journal of Physical Chemistry*
Manuscript ID	Draft
Manuscript Type:	Article
Date Submitted by the Author:	n/a

Complete List of Authors:	Mancini, Andrea; Universita degli Studi di Roma La Sapienza Dipartimento di Fisica, Physics Giliberti, Valeria; Istituto Italiano di Tecnologia Center for Life Nano Science; Sapienza University of Rome, Dipartimento di Fisica Alabastri, Alessandro; Rice University, Calandrini, Eugenio; Istituto Italiano di Tecnologia De Angelis, Francesco; Istituto Italiano di Tecnologia, Garoli, Denis; Istituto Italiano di Tecnologia, Ortolani, Michele; Sapienza University of Rome, Dipartimento di Fisica

SCHOLARONE™
Manuscripts

Thermoplasmonic Effect of Surface Enhanced Infrared Absorption in Vertical Nanoantenna Arrays

Andrea Mancini†, Valeria Giliberti‡, Alessandro Alabastri§, Eugenio Calandrini‖, Francesco De Angelis‖, Denis Garoli‖* and Michele Ortolani†*

† Dipartimento di Fisica, Sapienza University of Rome, Piazzale Aldo Moro 5, 00185 Rome, Italy

‡ Center for Life NanoSciences, Istituto Italiano di Tecnologia (IIT), Viale Regine Elena 291, 00185 Rome, Italy

§ Department of Physics and Astronomy and Department of Electrical and Computer Engineering, Rice University, 6100 Main Street, Houston, Texas 77005, United States

‖ Plasmon Nanotechnologies Department, Istituto Italiano di Tecnologia (IIT), 16163 Genoa, Italy

*corresponding author e-mails: denis.garoli@iit.it , michele.ortolani@roma1.infn.it

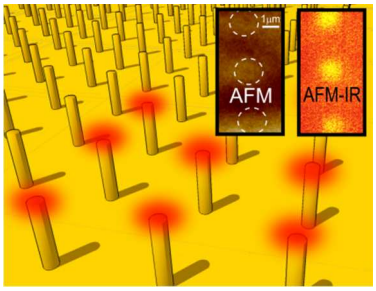

Abstract. Thermoplasmonics is a method for increasing temperature remotely using focused visible or infrared laser beams interacting with plasmonic nanoparticles. Here, local heating induced by mid-infrared quantum cascade laser illumination of vertical gold-coated nanoantenna arrays embedded into polymer layers is investigated by infrared nanospectroscopy and electromagnetic/thermal simulations. Nanoscale thermal hotspot images are obtained by a photothermal scanning probe microscopy technique with laser illumination wavelength tuned at the different plasmonic resonances of the arrays. Spectral analysis indicates that both Joule heating by the metal antennas and surface-enhanced infrared absorption (SEIRA) by the polymer molecules located in the apical hotspots of the antennas are responsible for thermoplasmonic resonances, i.e. for strong local temperature increase. At odds with more conventional planar nanoantennas, the vertical antenna structure enables thermal decoupling of the hotspot at the antenna apex from the heat sink constituted by the solid substrate. The temperature increase was evaluated by quantitative comparison of data obtained with the photothermal expansion technique to the results of electromagnetic/ thermal simulations. In the case of strong SEIRA by the C=O bond of poly-methylmethacrylate at 1730 cm^{-1}, for focused mid-infrared laser power of about 20 mW, the evaluated order of magnitude of the nanoscale temperature increase is of 10 K. This result indicates that temperature increases of the order of hundreds of K may be attainable with full mid-infrared laser power tuned at specific molecule vibrational fingerprints.

Keywords: plasmonics, nanoantennas, vibrational absorption, quantum cascade laser, atomic force microscope, surface-enhanced infrared absorption, photocatalyisis.

Introduction

Thermoplasmonics has emerged as a new way of increasing temperature remotely by light beams[1,2], exploiting the Joule heating effect at optical frequencies in metal nanoparticles[3-5] and nanoantennas[6-8]. Thermoplasmonics has been explored up to now with two different aims: (*i*) to produce a strong, local temperature increase ΔT at the nanoscale, in close proximity of single plasmonic nanoparticles in which light excitation results in high local currents hence strong power dissipation in the metal[4-7, 9-13]; or (*ii*) to increase the efficiency of radiation heating processes in large volumes or surfaces filled with both target molecules to be heated and plasmonic nanostructures acting as mediators of electromagnetic (e.m.) energy absorption for the entire system (global ΔT)[3,8,12]. The application of thermoplasmonic concepts has been carried out mostly with plasmonic nanoparticles randomly dispersed in solutions[3,4] or with single plasmonic antennas[6, 7], however antenna arrays have also been considered[14], because spatially coherent surface plasmon effects in periodic arrays may further enhance the absorption efficiency[15]. Remotely light-activated local or global temperature increases can be of extreme importance in e.g. catalysis[16,17], medical therapy[13, 18], material synthesis[10, 11], magnetic assisted recording[6], triggering of phase transitions[4,9], and thermophoresis[19].

The transient electron temperature at the metal surface of antennas in the field-enhancement regions can be far higher than the steady-state metal lattice temperature[1], leading to so-called hot electron effects such as electron tunneling emission[16,17,20]. Hot electron effects are distinct from Joule heating effect, although they may ultimately contribute to local and global heating. Following the pioneering work of Refs. 21-24, in this work we study a different path to thermoplasmonics based on e.m. energy dissipation by non-radiative decay of enhanced molecular dipole vibrations in the field-enhancement antenna hotspots. This mechanism of temperature increase is activated by laser illumination at substance-specific vibrational fingerprints in the mid-infrared (IR) range and belongs to the class of phenomena called surface-enhanced infrared absorption (SEIRA)[25,26]. In this work, we present nanoscale IR photothermal mapping of thermal hotspots in vertical antenna arrays embedded in polymer layers. In conjunction with e.m. and thermal simulations, the maps clearly show the existence of thermoplasmonic hotspots with strong temperature increase at the surface. Differently from thermoplasmonic systems operating in the near-IR and visible ranges, where dissipation in the metal is the only relevant heat source, in the mid-IR the contribution of molecular absorption can become important in determining the total temperature increase. In the context of mid-IR plasmonics, the novelty of our vertical antenna structures consists in the existence of an apical e.m. hotspot far from the solid substrate supporting the antennas, while in planar antenna structures all hotspots are very close to the substrate that operates as heat sink hence preventing the exploitation of the heat produced in the hotspots. Also, vertical antenna arrays feature high quality factor of the

resonances, which permits having spectrally distinct plasmonic resonance peaks that can be designed to overlap with different IR vibrations of molecules.

Organic molecule vibrations typically occur at molecule-specific frequencies in the "IR fingerprint" range 1000-2000 cm^{-1} (wavelengths between 5 and 10 μm), approximately covered by the tuning range of mid-IR external-cavity tunable quantum cascade lasers (EC-QCLs)[27] featuring power density high enough for thermoplasmonic applications. Indeed, temperature increase effects induced by mid-IR EC-QCL illumination have been recently exploited for applications such as mid-IR absorption nanospectroscopy of few molecules[28-30], nonlinear optics in the mid-IR based on phase transitions of liquid crystals[31], and mapping of both field-enhancement hotspots and currents in IR metamaterials[21-24, 32-33]. SEIRA has been long sought for in mid-IR plasmonic nanoantenna structures, however it has been elusive up to now due to Fano interference phenomena[34-40] that can prevent IR absorption enhancement while providing scattering enhancement[41,42]. One way to observe true absorption enhancement phenomena is to look at thermoplasmonic effects instead of scattering enhancement. The present work on vertical nanoantenna structures constitutes a complete analysis of thermoplasmonic effects therein, not only caused by conventional Joule dissipation, where metal nanostructures are the sources of heat[1-8], but also by SEIRA, where the molecules are the sources of heat[21-24].

Experimental Section

The vertical antennas consist in protrusions made of photoresist polymer spin-coated on a silicon wafer and then hardened by exposure to a focused ion beam. The non-exposed part of the film is removed in acetone. The resulting protrusions have a diameter of ~200 nm and a height *H* equal to the initial polymer film thickness. The fabrication process is entirely described in Ref. 43. The antenna arrays, including the flat silicon wafer surface, were coated conformally with a 80 nm thick evaporated gold film (thicker than 3 times the skin depth of gold in the mid-IR[44]), closing the access to the hollow cavity inside the protrusion and leading to a final gold-coated vertical rod antenna structure with diameter $d_{\mathrm{ant}} \sim 360$ nm [43,45]. The samples used in this work are square periodic arrays of vertical nanoantennas with *H* ranging from 2.2 to 2.7 μm and pitch *P* equal to 3.0, 3.5 or 4.0 μm. After fabrication, the vertical antennas were embedded up to their top in a spin-coated polymer bilayer film, so as to allow their nanoscale investigation by atomic force microscopy (AFM). The entire body of the antennas was embedded in a weak IR-absorber polymer (AZ5214, spin-coating speed 1000 to 2000 rpm, final thickness 3.1 to 2.1 μm). A thin layer of a strong IR-absorber polymer was spin-coated on top of the vertical antennas (PMMA 950k, 2% solids in ethyl-lactate, spin-coating speed 3000 to 2000 rpm, final thickness 100 to 400 nm), so as to fill the region where the apical antenna hotspots exist (i.e. those far away from the solid substrate acting as heat sink).

The mid-IR far-field response of the arrays is measured with a commercial Fourier-transform infrared (FTIR) spectrometer (*Bruker IFS66v/S*) coupled either to a home-made variable-angle reflection unit working with linearly-polarized radiation on large-area samples (about 1×2 mm^2), or to a reflective microscope (*Bruker Hyperion*), where quasi-unpolarized radiation is focused with a Cassegrain objective (incidence angle range of 10° to 30° with respect to the surface normal) onto a 70×70 μm^2 spot at the sample surface. A gold mirror is used as reference to compute the absolute reflectance $R_{s,p}(\omega)$ and the extinction is calculated as $1 - R_{s,p}(\omega)$ because transmission is zero, where the suffixes *s* and *p* refer to electric field polarization perpendicular and parallel to the incidence plane, respectively. Each spectrum is obtained as the average of 1024 interferometer scans at 4 cm^{-1} spectral resolution and the spectral range is 600 to 3000 cm^{-1}.

The nanoscale thermoplasmonic response of the system is investigated with an AFM operating in contact mode with the mechanical resonance-enhanced photothermal expansion technique (AFM-IR, *Anasys Instruments NanoIR2* with top side illumination)[28-30]. The mid-IR light source is a tunable EC-QCL (*Daylight Solutions MIRcat-PX-B*), with continuous wavelength (wavenumber) range of 5.5 to 9.1 μm (1900 to 1100 cm^{-1}) and accordable laser power range from 1 to 500 mW. To achieve full illumination of the probe tip, the laser beam impinges on the sample with a 70° angle with respect to the surface normal in *p*-polarization, leading to a Gaussian focal spot with elliptical footprint (major/minor axis with measured Gaussian width of 24/10 μm, see Supporting Information n.2) centered on the AFM probe tip. A laser power of 19 mW at 1730 cm^{-1} gives a laser power density in the focus of $1.7 \cdot 10^7$ W/m^2. The laser power varies within a factor of 3 in the tuning range of the EC-QCL. The AFM-IR photothermal expansion maps are obtained by monitoring the AFM probe cantilever deflection oscillations at the repetition rate of the EC-QCL, which is set to match the mechanical resonance of the cantilever (here, 220 kHz). The voltage scale V_{PSPD} of the presented AFM-IR maps and spectra is the AFM position-sensitive photodetector signal component at the EC-QCL repetition rate of 220 kHz, measuring the laser-induced AFM cantilever deflection oscillations[30]. The AFM topography maps are simultaneously recorded from the dc component of the deflection signal. The laser pulse duration is 260 ns, the duty cycle is 6%. The spectral resolution is 2 cm^{-1}. Uncoated silicon probe tips with slanted tip shaft (*Nanosensors AdvancedTEC*) were employed to avoid perturbation of nanoantenna fields (see Supporting Information n.1).

The e.m. simulations were performed using the commercial software COMSOL Multiphysics. Calculations were carried out by placing the antennas (described by a Drude-Lorentz electric permittivity[44]) on a metal half-space and filling the other half-space with a background medium (refractive index 1.6) up to the antenna height and placing air (refractive index 1) elsewhere. An absorbing PMMA layer, 100 nm thick, was located between air and top antenna plane. The fabricated and experimentally characterized samples were modeled as infinite three-dimensional arrays of antennas where Floquet periodic conditions were set in the planar directions to define the rectangular unit cells. Input radiation was accounted for by setting e.m. ports at the top surface of the modeled

domain, on the interior side of the perfect matching layer, setting an angle of incidence θ_{inc}. The incident radiation was represented by a linearly polarized plane wave, the absorption and scattering spectra were obtained, and the field enhancement maps were then calculated at the plasmonic resonance frequencies derived from the simulated spectra.

Results and Discussion

In Figure 1a-b SEM images of the samples before the polymer embedding procedure are shown. The antennas are constituted by gold-coated vertical cylinders protruding from a flat surface, also gold-coated. The geometrical parameters (height *H* and array pitch *P*) were chosen on the basis of previous work[45] so as to overlap the plasmonic resonance frequencies in the mid-IR range with the molecular vibration frequencies of the two different polymers (AZ and PMMA) embedding the vertical antennas. As a further fine-tuning parameter for obtaining better frequency overlap, the vertical antennas were also fabricated with a tilt angle $\theta_{\mathrm{tilt}} = 10°$ or $20°$ with respect to the surface-normal direction. The tilt angle acts as a small perturbation of the plasmonic modes of the array, whose resonance frequency is mainly set by *P* and *H* and by the incidence angle θ_{inc} of the illuminating IR beam. In Figure 1c, the plasmonic mode structure of the bare samples is investigated by variable incidence-angle FTIR reflection spectroscopy. The *p*-polarized reflectivity R_{p} (radiation electric field partly parallel to the antenna axis) shows dips at plasmonic mode frequency, corresponding to extinction peaks, not seen in the *s*-polarized reflectivity R_{s} (radiation electric field orthogonal to the antenna axis). Starting form almost-normal incidence ($\theta_{\mathrm{inc}} = 10°$), two modes appear in the R_{p} spectra, which we call bright modes at frequencies ω_{1b} and ω_{2b} almost independent on the incidence angle. At strongly non-normal incidence, a mode with angular dispersion appears, activated by asymmetry of the illumination direction. Therefore, we call this mode the asymmetric mode. The bright modes have an intrinsic dipole moment related to the antenna structure, while the asymmetric mode is a "spoof" surface plasmon mode related to the periodic array structure (see Supporting Information n.5). The vertical antenna arrays were then embedded in polymers and investigated by AFM-IR[28-30], a technique suitable for mapping the local photothermal expansion in the nanoscale antenna hotspots (see an example in inset of Figure 1a)[21-24, 32-33, 46].

E.m. absorption maps and temperature maps have been determined by 3D numerical simulations, reported in Figures 1d-f for a typical resonance condition where both the plasmonic nanostructure and the top molecular layer (PMMA) separately present a maximum in the e.m. response. In Figure 1d, the e.m. absorption is plotted in logarithmic scale using the absorption A_0 of the same PMMA layer without antennas as reference value. It is clear that both the vibrational absorption of the PMMA molecules and the ohmic losses of the metal antenna can generate comparable amounts of heat. For the PMMA molecules located in the apical antenna hotspot, the absorption is locally enhanced by several orders of magnitude (SEIRA effect), as highlighted in Figure 1e, where

the same simulation of Figure 1d is presented with shifted color scale. In Figure 1f, the resulting temperature map is shown: due to combined effect of the large distance of the apical hotspot from the substrate heat sink and of high thermal conductivity of gold, the ΔT along the antenna shaft is much smaller than the $\Delta T_{\max}$ of the PMMA molecules in the thermal hotspot, reaching up to $\Delta T_{\max} \approx 20$ K for 19 mW of laser illumination power at the C=O stretching vibration of PMMA. Air molecules in the vicinity of the thermal hotspot are also heated considerably, as already reported for vertical antenna arrays[8]. Elsewhere, ΔT is below 3 K.

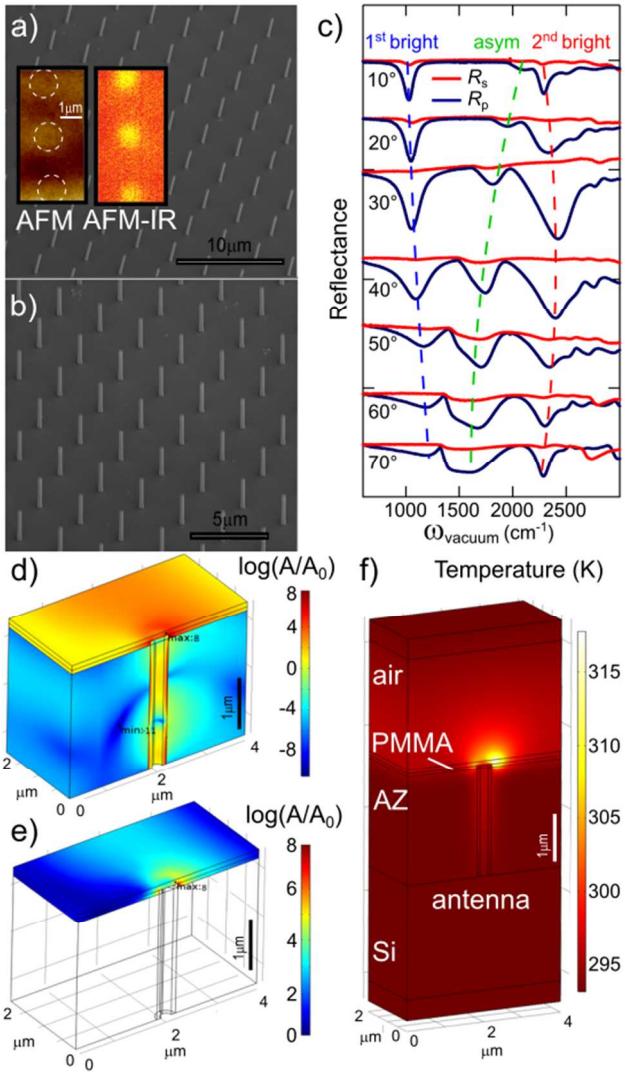

Figure 1. a-b) Scanning electron micrographs of an array of vertical antennas, with 10° tilt angle in a) and with zero tilt angle in b). Insets of panel a) AFM topography and AFM-IR photothermal expansion image of a portion of the array embedded into a polymer bilayer. c) Variable incidence angle reflectance spectra of the antenna arrays. Plasmonic resonances appear in the *p*-polarized spectra covering the entire mid-IR vibrational absorption range of organic molecules. d) E.m. simulations at θ_{inc} = 70°of the local electromagnetic absorption in a sample geometry giving a plasmonic resonance that matches the frequency of the strong C=O stretching vibration of PMMA. e) Same as d) but with different color scale, and map limited to the PMMA layer, to make SEIRA in the antenna hotspot more evident. f) Thermal simulations of the temperature reached by each point at the end of the mid infrared laser pulse for 19 mW of laser illumination power, using the absorption in d) as heat source. The air layer at the top of the cell and the Si substrate at the bottom are set as heat sinks at 293 K.

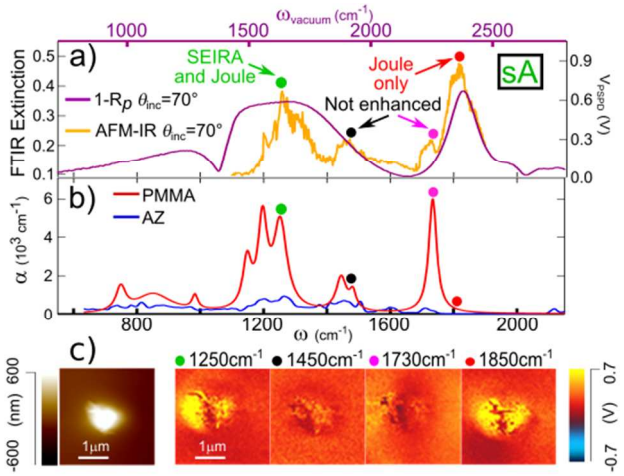

Figure 2. a) FTIR extinction spectrum in *p*-polarization of sample sA without polymers measured at $\theta_{inc} = 70°$, and AFM-IR spectrum with embedding polymers; the FTIR extinction is plotted vs. $\omega_{vacuum} = n\omega$ with $n = 1.3$ (see text). b) Absorption coefficients of the embedding polymers PMMA and AZ measured by FTIR. c) Topography and AFM-IR maps of a single antenna of sample sA at the IR vibration frequencies indicated by the color dots in the spectra (green, 1250 cm^{-1}, C-O-C stretching; black, 1450 cm^{-1}, C-H bending; pink, 1730 cm^{-1}, C=O stretching; red, 1850 cm^{-1} no vibrational fingerprint). The plasmonic mode at $\omega = 1850$ cm^{-1} generates heat only through the Joule effect, while the plasmonic mode at $\omega = 1200$-1400 cm^{-1} generates heat by both the Joule effect and the SEIRA effect. At $\omega = 1450$ cm^{-1} and 1730 cm^{-1} heat is generated only via Beer-Lambert absorption by polymers.

IR spectroscopy and nanoimaging data are reported in Figure 2 for sample sA with $H = 2.7$ μm. In Figure 2a, the FTIR extinction spectrum at $\theta_{inc} = 70°$ of the antenna array (violet curve) is shown together with the AFM-IR spectrum acquired by continuously tuning the EC-QCL wavelength with the probe tip position kept fixed on top of a single antenna (orange curve, also measured at $\theta_{inc} = 70°$). Embedding the structure in the polymer bilayer results in a redshift of the resonances by a factor n approximately equal to the square root of the effective dielectric permittivity of the environment, so the FTIR extinction measured before embedding the antennas is plotted vs. the top axis $\omega_{vacuum} = n\omega$. Both scattering and absorption losses determine the FTIR extinction spectrum, but only the absorption losses contribute to ΔT hence to the AFM-IR signal, because in general the e.m. energy of scattering losses is radiated away from the system. Indeed, it has been recognized that transmission/reflection spectroscopy is not suitable to isolate thermoplasmonic effects among other plasmonic field-enhancement effects[38]. Several techniques have then been developed to directly measure the thermoplasmonic ΔT at the nanoscale[7, 47-50]. AFM-IR measures the photothermal expansion of the material under a scanning probe tip, which ultimately depends on the absorption only[21-24, 28-30]. While AFM-IR is not always suitable to determine the absolute ΔT [51], it features nanoscale mapping resolution for imaging the local photoexpansion in plasmonic resonators beyond the diffraction limit [21-24, 32, 33]. By scanning the probe tip at fixed laser wavelength on the surface of the embedding polymer layer, photoexpansion maps such as those in Figure 2c can be acquired and then used to study heat fluxes at the nanoscale.

Looking at the molecular absorption spectra of the embedding polymers reported in Figure 2b, AZ can be considered as a weak IR absorber, while PMMA is a well-known strong IR absorber at the three main molecule absorption bands around 1150-1250, 1450 and 1730 cm^{-1} corresponding to C-O-C stretching, C-H bending and C=O (carbonyl) stretching vibrations, respectively. Frequency overlap of the PMMA vibrations with the plasmonic modes of the vertical antenna arrays (a necessary requirement for SEIRA) is summarized in Figure 2

by color dots. In Figure 2a, a strong thermoplasmonic peak is observed in the AFM-IR spectrum at 1850 cm^{-1} (red dot), where there is no molecular vibration, and it is therefore attributed to Joule heating at the 2nd bright plasmonic mode at ω_{2b}. The small offset between the peak frequency in $1 - R_p(\omega)$ and that in the AFM-IR spectrum around 1850 cm^{-1} is due to the difference in resonance frequencies between far-field and near-field detection of the plasmonic antenna resonance[52]. Besides the bright mode peak at 1850 cm^{-1}, in Figure 2a the asymmetric plasmonic mode is observed in the AFM-IR spectrum at 1250 cm^{-1} (green dot), with a clear counterpart in the corresponding $1 - R_p(\omega)$. The peak at 1250 cm^{-1} also corresponds to the C-O-C stretching vibration of PMMA, leading to an increase of the molecular dipole absorption strength (SEIRA) if compared e.g. to the non-enhanced vibration at 1730 cm^{-1} (pink dot). Interestingly, in sample sA at 1250 cm^{-1} one directly observes the thermoplasmonic effect of SEIRA in the AFM-IR spectrum[21-24], and not just its consequences in the reflection spectrum, typically resulting in asymmetric Fano lineshapes[26]. Note that the high quality factor of plasmonic resonances in vertical antenna arrays allows for the visualization of both modes separately in the same AFM-IR spectrum.

The photothermal expansion maps at 1850 cm^{-1} (Joule heating only) and at 1250 cm^{-1} (both SEIRA and Joule heating) are reported in Figure 2c for sample sA: therein, nano-thermal hotspots are clearly detected[21-24, 32-33, 46]. In the control experiments at the molecular absorption frequencies of 1450 cm^{-1} and 1730 cm^{-1} (black and pink dots respectively), in the absence of plasmonic field enhancement the maps of Figure 2c do not show any thermal hotspot, because heat is generated everywhere on the sample surface by direct molecular absorption (Beer-Lambert). The thermal hotspots seen in the AFM-IR maps of Figure 2c at 1850 cm^{-1} and 1250 cm^{-1} display half-width half-maximum diameters around 600 nm. In vertical nanoantennas, the field-enhancement regions (i.e. the e.m. hotspots) are only slightly broader than d_{ant} ~ 360 nm [40,43,45]. The difference between the hotspot size measured with AFM-IR imaging (600 nm) and the e.m. hotspot size (< 400 nm) is to be attributed to the effect of thermal diffusion in polymers[28-30, 51].

In Figure 3a the FTIR extinction at different θ_{inc} is reported for sample sA and in Figure 3b the e.m. spectral simulations of the total absorption are shown for comparison. The two bright modes and the asymmetric mode are clearly seen in both spectroscopy and e.m. simulations. The bright modes can be straightforwardly identified as localized plasmon oscillations corresponding to 1st and 2nd order dipole resonances of the vertical rod, including the length doubling effect of the mirror dipole produced by the ground plane[45] (see Supporting Information n. 4). In Figure 3c the angular dispersion of the mode frequency is reported for sample sA. The asymmetric mode frequency approximately follows the "spoof" surface plasmon dispersion law in the mid-IR for a square array $\omega(\theta) \cong 2\pi c/P(1 + \sin\theta)$ (green continuous line)[45] where c is the light velocity implementing the effective dielectric permittivity factor n. All other samples were measured only at $\theta_{inc} \approx 20°$ in the microscope and at $\theta_{inc} = 70°$ in the AFM-IR. In Figure 3c, the fine tuning effect of the tilt angle can be

observed for samples sB and sD (see Table 1 for all geometrical parameters and resonance frequencies of all samples). Fine tuning of the plasmonic mode frequencies is crucial to obtain resonance with the different PMMA vibrations, indicated by dashed lines in Figure 3c. Sample sC has lower antenna height $H = 2.2$ μm than the other samples ($H = 2.7$ μm), therefore all resonances are blueshifted approximately by the height ratio, and the asymmetric mode resonates with the C=O stretching vibration of PMMA at 1730 cm^{-1}.

In Figure 3d and 3e the simulated field-enhancement maps for the asymmetric mode and the 2nd bright mode of a structure with geometrical parameters identical to sample sA are reported for $\theta_{\mathrm{inc}} = 70°$, which is the illumination condition for the AFM-IR setup. The maps in Figure 3d and 3e confirm the existence of e.m. hotspots at the apex of the rod and of additional field enhancement regions along the shaft. More precisely, the highest field intensity is reached in a circumference corresponding to the apical rim of the antenna (see also Figure 5d). The molecules contained in these field enhancement regions undergo enhanced mid-IR absorption (SEIRA) contributing to generate a local ΔT, which is estimated here through the consequent photothermal expansion.

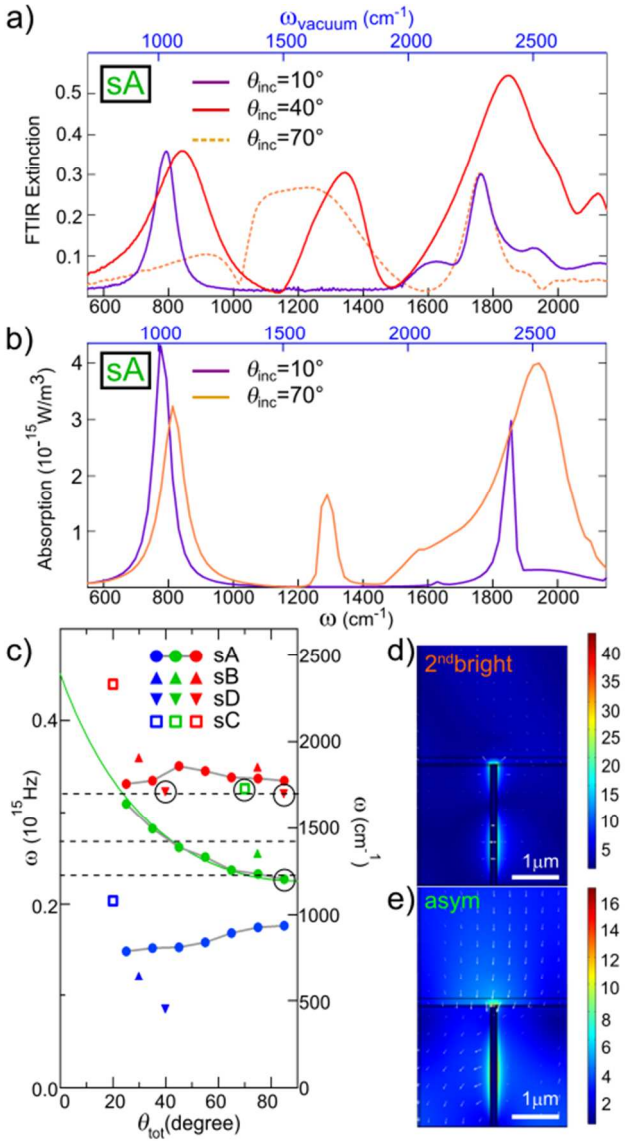

Figure 3. Plasmonic modes of sample sA1 with $H = 2.7$ μm and $P = 4.0$ μm. a) Experimental FTIR reflection data and b) simulated absorption spectra at different θ_{inc}. The simulated spectrum for $\theta_{inc} = 70°$ is the average of spectra calculated for $60° \leq \theta_{inc} \leq 80°$ (see Supporting Information n. 3). c) Measured plasmonic mode frequency as a function of θ_{tot} for all samples. The green continuous line represents the expected dispersion of a "spoof" surface plasmon polariton. Blue symbols: 1st bright mode. Green symbols: asymmetric mode. Red symbols: 2nd bright mode. Note that sample sC has $H = 2.2$ μm, others have $H = 2.7$ μm. Dashed lines: frequencies of PMMA vibrations. Black circles indicate resonance of plasmonic modes with PMMA vibrations. The total angle θ_{tot} approximately accounts for the quasi-dipole excitation pattern of the vertical antennas that select a specific illumination angle, relative to the vertical antenna axis, within the broad angular distribution of the optical objectives employed in the experiments. d), e) Simulated field enhancement maps for sample sA2, showing an apical hotspot for both asymmetric and bright plasmonic modes.

Sample	***H*** (μm)	θ_{tilt}	***P*** (μm)	ω_{1b} (cm^{-1})	ω_{asym} (cm^{-1})	ω_{2b} (cm^{-1})
sA	2.7	0°	4.0	780	1240	1820
sB	2.7	10°	3.5	640	1350	1850
sC	2.2	0°	3.5	1080	1730	2330
sD	2.7	20°	3.0	450	1050	1700

Table 1. Geometrical parameters and experimental plasmonic mode frequencies of the investigated samples. ω_{1b} , ω_{asym} , ω_{2b} indicate the frequency of the 1st bright, asymmetric and 2nd bright plasmonic modes of embedded samples (experimental values obtained by FTIR microspectroscopy).

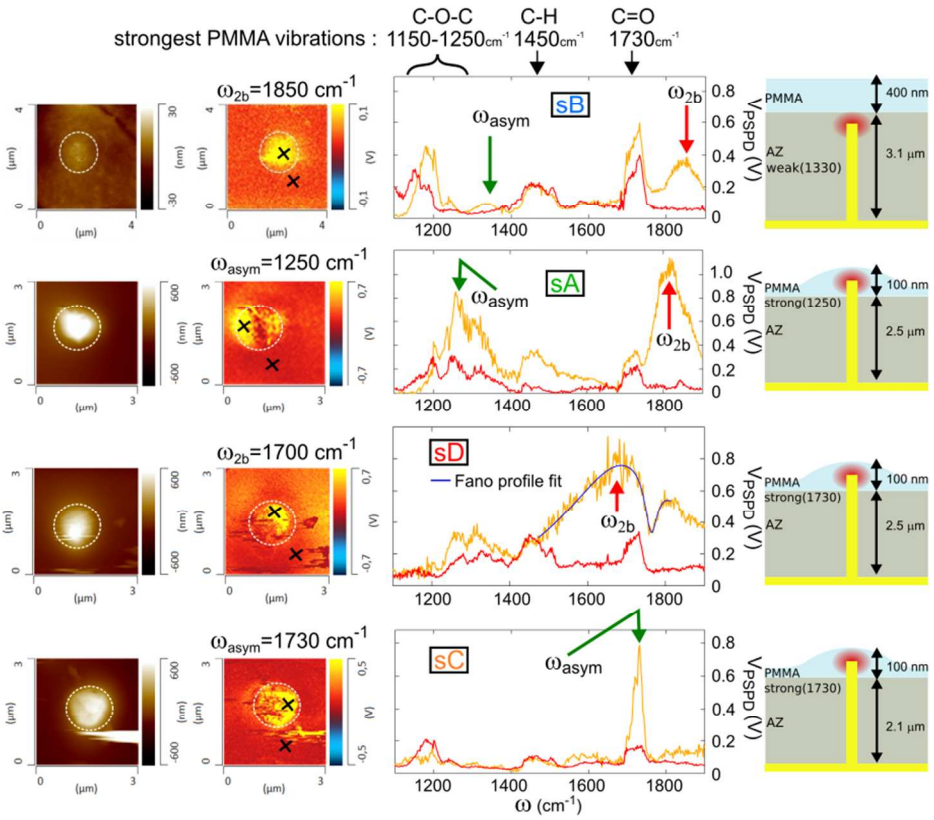

Figure4. From left to right column: AFM topography map, AFM-IR photothermal expansion map, AFM-IR spectra in two different locations (outside and inside the hotspots) and sketch of the embedding polymer configuration. Data for four samples are reported in the four different rows (sample parameters reported in Table 1). The AFM-IR maps (red-hot color scale) are taken at different plasmonic mode frequency, as specified above each map. In the sketches on the right, the embedding polymer bilayer thicknesses are reported with the strengths and frequencies (in cm^{-1}) of specific molecule vibrations enhanced by the asymmetric mode of each sample (green arrows in the spectral plots).

In Figure 4 a full set of experimental AFM-IR spectra and maps is shown for different samples: sB (control sample, plasmonic modes not resonant with molecular vibrations), sA (both SEIRA and Joule effect), sD (strong Joule effect) and sC (strong SEIRA effect). From left to right in Figure 4, one can see for each sample the AFM topography maps (sepia color scale), the corresponding AFM-IR maps (red-hot color scale), the AFM-IR spectra at two locations (one in the antenna hotspot, orange curve, and one outside the hotspot, red curve), and the sketch of the embedding polymer bilayer configuration with thickness values. In the control sample sB, in which thicker embedding layers were used in order to displace the PMMA molecules 400 nm away from the hotspot, the AFM-IR spectrum in the hotspot (orange curve) displays a peak at ω_{2b} = 1850 cm^{-1} originating from Joule heating by the 2nd bright mode (first line of Figure 4). The asymmetric mode appears in the same curve as a small Joule heating peak at 1330 cm^{-1}, due to the absence of strong IR vibrations in the AZ molecules. Comparing the relative intensity of the PMMA vibrations at 1150-1250, 1450 and 1730 cm^{-1} in sample sB, one sees that they are identical for both the orange and the red curve, and also that they match the ratio 2:1:2 measured in the absence of plasmonic field enhancement (see Figure 2b for reference). In the AFM-IR spectra of samples sA, sD and sC, instead, the spatial overlap of the apical hotspot with the PMMA layer produces a

resonant coupling of the plasmonic modes with the strong molecular vibrations of PMMA. In the spectrum of sample sA, already discussed in Figure 2, a pure Joule heating peak related to the 2nd bright mode is present around ω_{2b} = 1850 cm^{-1}, where PMMA displays no vibrational absorption. The asymmetric mode of sA instead resonates with the PMMA vibration at 1250 cm^{-1}: as a result, the peak intensity ratio in the orange curve of sample sA is approximately 4:2:2, indicating a two-fold enhancement of the peak at 1250 cm^{-1}. In sample sD, the 2nd bright mode resonates with the PMMA vibration at 1730 cm^{-1} leading to an asymmetric Fano lineshape in the AFM-IR spectrum (see below), which prevents the definition of a peak intensity ratio. In sample sC, the bright modes lie outside the AFM-IR frequency range (see Table 1), while the asymmetric mode at 1730 cm^{-1} resonates with the C=O stretching vibration of PMMA, producing a remarkable seven-fold enhancement of the AFM-IR signal (peak intensity ratio is 2:1:14). Note that the normal PMMA peak intensity ratio of 2:1:2 is well reproduced not only in the control sample sB, but also in all spectra taken outside the antenna hotspots (red curves). The seemingly low spectral quality of AFM-IR data is due to poor adhesion of the top PMMA layer to the bottom AZ layer, and therefore this spectral quality is specific to the present sample structure and should not be regarded as the typical signal-to-noise ratio of the AFM-IR technique.

The different situation that arises in sample sD deserves some more comment. Therein, the 2nd bright mode is centered at 1700 cm^{-1} and partially overlaps with the strong vibration of PMMA at 1730 cm^{-1}. As it is well known[34-40], the resonance overlap leads to a characteristic Fano interference lineshape in the extinction spectra which, being a near-field interference phenomenon, has an absorptive counterpart that can be observed in the AFM-IR spectra[53]. In other words, the dip at 1755 cm^{-1} in Figure 4 (third line) is the result of destructive interference between the enhanced field of the plasmonic bright mode and the polarization field of the narrow PMMA vibration[42,54]. Apparently, these two fields reach a phase difference close to π at 1755 cm^{-1} in sample sD. As a result, the molecule absorption is not efficiently enhanced in the antenna hotspot, and the total thermoplasmonic energy dissipation is even lower than in the absence of a molecular vibration. The bright mode lineshape is a quasi-continuum if compared to the narrow PMMA vibration, so the AFM-IR absorption lineshape could be reproduced by a Fano model taken from Ref. 40 (blue curve in third line of Figure 4). We recall that the occurrence of Fano interferences is the main reason why a true SEIRA phenomenon was seldom observed in mid-IR nanoantennas[34-40, 55], and the concepts of surface enhanced infrared scattering (SEIRS) or of resonant SEIRA have been developed instead[26]. The quasi-Lorentzian lineshape seen in the case of SEIRA induced by the asymmetric mode (sample sC) can be interpreted within the same Fano resonance model as a weak coupling between antennas and molecules. In summary, Figure 4 shows that the strength of the antenna-molecule interaction and the relative heating contribution by Joule and SEIRA effects are specific to the given sample structure and to the related plasmonic mode structure.

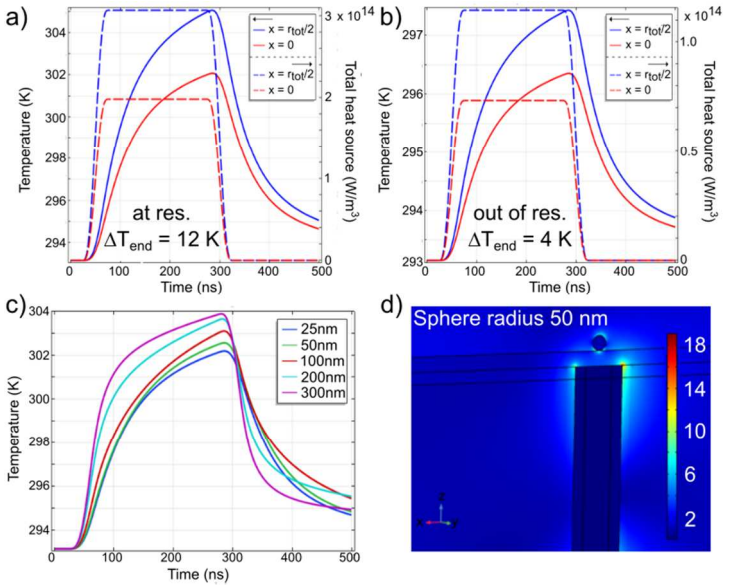

Figure 5. a), b) Time dependence of the absorption at 1730 cm^{-1} (dashed lines, right scales) representing the local heat source, and of the temperature (continuous lines, left scales). Red and blue lines refer to values above the antenna center and above the antenna rim respectively. In a) the thermal dynamics in the case of resonance between plasmon and vibrations is shown (structure similar to sample sC), while in b) the plasmonic resonance is slightly detuned by increasing the array pitch P = 3.5 μm to P = 5.0 μm. Note the different scales in the two plots. c) Time dependence of the temperature above the antenna center with silicon spheres of varying radius located on top of the polymer layer, representing the scanning probe tip apex that generates weak e.m. and thermal perturbations. d) Field enhancement map at the antenna apex with a silicon sphere of radius 50 nm is reported as an example.

We now turn to the quantitative determination of the ΔT in different locations of our samples at the SEIRA frequency ω_{SEIRA}. We focus on the structure of sample sC at two types of locations: points of the sample surface above the center of the antenna and points above the antenna rim where the e.m. hotspots are located, reaching a slightly higher local temperature $T_{\mathrm{hs}}(\omega_{\mathrm{SEIRA}})$ under laser illumination with power density 1.7·10^7 W/m^2 at 1730 cm^{-1}. The points at the surface of the embedding layer at a distance ~P/2 from the antenna hotspot (red pixels in the AFM-IR maps of Figure 4), are subject to a much smaller global ΔT from the laboratory temperature of 293 K to a slightly higher $T_{\infty}(\omega_{\mathrm{SEIRA}})$. The dynamic thermal simulation of the temperature of such locations during the laser pulse are reported in Figure 5a for the structure of sample sC at the SEIRA frequency ω_{asym} = 1730 cm^{-1} matching the strongest PMMA vibration, and in Figure 5b for a nonresonant structure (pitch P increased to 5 μm). In Figure 5a, one obtains $T_{\mathrm{hs}}(\omega_{\mathrm{SEIRA}})$ = 305 K above the antenna rim at $x = \frac{d_{\mathrm{ant}}}{2} = 180$ nm (where x is the distance from the antenna center along the illumination direction) or $\boldsymbol{\Delta T_{\mathrm{hs}}(\omega_{\mathrm{SEIRA}}) = 12}$ **K.** Above the antenna center (red curve in Figure 5a), one observes very similar temporal dynamics but $\Delta T(\omega_{\mathrm{SEIRA}}) = 9$ K. This is due both to the heat source (e.m. hotspots) being located at the antenna rim and to the thermal conduction through the metal antenna creating a minimum in the temperature increase at $x = 0$. Indeed, for the same reason an even higher $\Delta T_{\mathrm{max}} \approx 20$ K is obtained for the PMMA molecules located 100 nm outside the antenna rim (see Figure 1f). From Figure 1f, one also sees that the global temperature increase far from the hotspot $\Delta T_{\infty}(\omega_{\mathrm{SEIRA}})$ is below 3 K and therefore $\Delta T_{\mathrm{hs}}(\omega_{\mathrm{SEIRA}})$ is significantly higher (four times higher than the global increase, as also derived from the quantitative analysis of the spectra in Figure 4). Figure 5a and 5b also demonstrate that the employed laser pulse duration of 260 ns and the much longer repetition time of ~ 4.5 μs result in a quasi-equilibrium temperature being approximately reached after each laser pulse[30], as required by the resonantly-enhanced photothermal expansion version of AFM-IR used here [56, 58].

Due to the large uncertainties related to the thermal material parameters employed in the simulations, we have used the experimental data to confirm the simulated value of $\Delta T_{\mathrm{hs}}(\omega_{\mathrm{SEIRA}})$ in two different ways: (*i*) from an independent calibration of our instrument-sample configuration, fully reported in the Supporting Information n. 7, in which the top PMMA layer of our embedded antenna structure is substituted by a different material (hydrogen-silsesquioxane, HSQ) displaying a temperature-dependent intensity of a specific vibrational absorption line[59] working as a "local thermometer"; from the calibration plot in Figure S7, we calculate for sample sC a $\boldsymbol{\Delta T_{\mathrm{hs}}(\omega_{\mathrm{SEIRA}}) \approx 17 \pm 6\ \mathrm{K}}$; and (*ii*) from the observed absolute value of V_{PSPD} reported in the spectra of Figure 4, using the thermo-mechanical model for resonantly-enhanced photothermal expansion of Ref. 30. By following the procedure of Ref. 30, the variation $\Delta\delta$ of the indentation depth δ during each laser pulse (photoexpansion length) is considered as the main mechanism of impulse transfer from the material to the cantilever through the probe tip. The value of the cantilever deflection signal induced by photoexpansion V_{PSPD} can then be used to calculate $\Delta T_{\mathrm{hs}}(\omega_{\mathrm{SEIRA}})$ under the assumption that only the PMMA layer undergoes a significant ΔT, and therefore it is the only portion of the sample that undergoes photothermal expansion, as indeed indicated by the thermal simulations (see Figure 1f). Further, we simplify the calculation by assuming a homogeneous ΔT for the layer contained in a cylinder extending between the antenna and the AFM tip apex, with height h = 100 nm and circular base radius equal to the thermal diffusion length around 300 nm as seen in both simulations and AFM-IR imaging (see maps in Figures 2 and 4)[28,29,51,56]. Details of the calculation and material parameters are reported in the Supporting Information n.6, but briefly, from the maximum experimental value of $V_{\mathrm{PSPD}} \sim 1.0$ V and the measured mechanical quality factor of our AFM-IR cantilevers of 113, we obtain $\Delta\delta \simeq 4{,}7 \cdot 10^{-11}$ m. Neglecting the thermal expansion of the gold-coated nanoantenna, which is justified for significant molecular heating at $\omega = \omega_{\mathrm{SEIRA}}$, and using a linear thermal expansion coefficient $\ell = 7 \cdot 10^{5}\mathrm{K}^{-1}$ for PMMA, we obtain a local $\boldsymbol{\Delta T_{\mathrm{hs}}(\omega_{\mathrm{SEIRA}}) = \Delta\delta/(\ell h) = 7 \pm 3\ \mathrm{K}}$, which just confirms the order of magnitude of the temperature increase obtained from the simulations of Figure 5 and the calibration with the HSQ layer.

Finally, one may ask whether the presence of the AFM-IR probe affects the thermal dynamics and the obtained ΔT in the antenna hotspot. We recall that we have used uncoated silicon probe tips so as to reduce the e.m. interaction of the tip with the plasmonic resonances. In Figure 5c, we show the thermal simulations of the same structure of Figure 5a with a silicon sphere of varying radius added on top of the antenna, representing the AFM probe tip. The actual curvature radius of our probes is around 25 nm and their shape is that of a trigonal pyramid, so the silicon sphere only models the probe tip apex. In Figure 5d, the e.m. simulations are shown and indicate that the hotspot pattern is not significantly modified by the presence of a silicon probe tip (compare Figure 5d to Figure 3e). The absorption in silicon at 1730 cm^{-1} is negligible with respect to that of PMMA and gold. The ΔT inside the spheres is negligible for any considered sphere radius, because the thermal conduction link with the heated PMMA layer is reduced to air flow and to a very small contact point. This indicates that the ΔT of

PMMA does not depend on the presence of a silicon probe tip on top of it, and that the thermal expansion of the probe tip can be neglected in the calculations of ΔT_{hs}. In Figure 5c, one also sees a slightly higher ΔT of the PMMA layer for larger spheres, despite the increase of the total heat capacity. The latter effect can be understood as an increase of the field enhancement in the nanogap between the antenna apex and the sphere with increasing scattering cross section of the sphere (related to the increasing sphere radius). Note that the probe tip was not included in the full e.m. and thermal simulations of Figure 1 and 5, however its effect is certainly included in the experimental calibration performed with the HSQ layer, which leads to similar values of $\Delta T_{\mathrm{hs}}(\omega_{\mathrm{SEIRA}})$.

The fact that calibrations, simulations and calculations starting from V_{PSPD} provide values of ΔT_{hs} of the same order of magnitude around 10 K guarantees that the thermoplasmonic effect of the probe tip is a second-order correction, and that the vertical antenna structure could be employed outside the AFM-IR setup for thermoplasmonic applications, as already suggested in Ref. 8. The presented structures could then be exploited for laser-assisted catalysis of chemical reactions involving molecular species immobilized on the surface of the antennas[16, 17] and also for efficient global heating of macroscopic sample surfaces with narrowband laser light at the mid-IR vibrational resonance of given molecules, employing continuous-wave QCLs. If compared to broadband mid-IR perfect absorbers, such as carbon black, nanoporous gold[40], or metasurfaces[15,60,61], the vertical antenna arrays presented in this work can be substance-selective when operated at mid-IR wavelengths for which SEIRA is dominant over Joule heating (see e.g. sample sC at 1730 cm^{-1}). In general, the additional thermoplasmonic effect of SEIRA by molecules, beyond that of Joule heating by metals, occurs in the mid-IR when molecules with vibrational fingerprints resonant with plasmonic modes are present in the antenna hotspots, effectively producing a kind of "mid-IR chemical trigger" of the thermoplasmonic ΔT.

Conclusions

We have measured the thermoplasmonic response in the mid-infrared of vertical antenna arrays embedded into polymer layers by using a scanning probe microscopy technique based on the photothermal expansion effect. We have investigated specific surface-enhanced infrared absorption (SEIRA) conditions in different arrays, in which the molecule vibrations resonate with the plasmonic modes of the antennas in the mid-infrared. Illumination was provided by a wavelength-tunable quantum cascade laser and resonance conditions between molecular absorption and plasmonic modes could be achieved thanks to the high quality factor of the plasmonic resonances featured by vertical antenna arrays. The vertical antennas were embedded in a polymer layer of thickness slightly larger than the antenna height so as to spatially overlap the apical antenna hotspot with the top polymer layer, thereby strongly reducing the thermal conduction link between the heated molecules and the substrate heat sink if compared to previous similar works on planar antenna structures.

The study of the photoexpansion spectra measured with the scanning probe tip positioned above the antenna apex has demonstrated plasmon-enhanced molecule vibration intensities that non-radiatively decay into heat. The absolute temperature increase in our experiment was estimated by thermal simulations, by an experimental calibration and by scanning probe sensitivity calculations to be in the range 7 K to 20 K with 19 mW of focused mid-infrared laser illumination at a wavelength of 5.8 μm (1730 cm^{-1}). The perturbation of the antenna modes by the scanning probe tip is found to be minimal, therefore the antenna structures could be used independently for thermoplasmonic applications. Using focused beams from modern quantum cascade lasers at their maximum full emission power surpassing 1 W, it should be possible to reach local thermoplasmonic temperature increases of hundreds of Kelvin degrees by locating in the antenna hotspots specific molecules, whose mid-infrared vibrational fingerprints resonate with the plasmonic modes of the vertical antenna arrays.

Acknowledgements. A.M. and M.O. authors acknowledge support from Sapienza University of Rome, "Ateneo 2017 – H2020" grant and from the Italian Ministry of University and Research (MIUR) through program PRIN 2015FSHNCB

The **Supporting Information file** contains figures and text on: 1. Experiments with gold-coated probe tips; 2. Evaluation of laser power density; 3. Simulated quality factor of the asymmetric mode; 4. Interpretation of the bright modes as linear dipole resonances; 5. Interpretation of asymmetric array modes as spoof surface plasmons; 6. Temperature increase evaluation at SEIRA condition; 7. Temperature increase calibration with the HSQ vibrational peak.

References

[1] Baffou, G.; Quidant, R. Thermo-plasmonics: Using Metallic Nanostructures as Nano-Sources of Heat. *Laser Photonics Rev.* **2013**, *7*, 171-187.

[2] Evans, C. I.; Zolotavin, P.; Alabastri, A.; Yang, J.; Nordlander, P.; Natelson, D., Quantifying Remote Heating from Propagating Surface Plasmon Polaritons. *Nano Lett.* **2017,** *17* (9), 5646-5652.

[3] Govorov, A. O.; Richardson, H. H. Generating Heat with Metal Nanoparticles. *Nano Today* **2007**, *2*, 30-38.

[4] Adleman, J. R.; Boyd, D. A.; Goodwin, D. G.; Psaltis, D. Heterogenous Catalysis Mediated by Plasmon Heating. *Nano Lett.* **2009**, *9*, 4417-4423.

[5] Alabastri, A.; Tuccio, S.; Giugni, A.; Toma, A.; Liberale, C.; Das, G.; De Angelis, F.; Di Fabrizio, E.; Proietti Zaccaria, R., Molding of Plasmonic Resonances in Metallic Nanostructures: Dependence of the Non-Linear Electric Permittivity on System Size and Temperature. *Materials* **2013,** *6* (11), 4879-4910.

[6] Stipe, B. C.; Strand, T. C.; Poon, C. C.; Balamane, H. ; Boone, T. D.; Katine, J. A.; Li, J.-L.; Rawat, V.; Nemoto, H.; Hirotsune, A.; Hellwig, O.; Ruiz, R.; Dobisz, E.; Kercher, D. S.; Robertson, N.; Albrecht, T. R.; Terris, B. D. Magnetic recording at 1.5 Pb m^{-2} Using an Integrated Plasmonic Antenna. *Nat. Photonics* **2010**, *4*, 484– 488.

[7] Coppens, Z. J.; Li, W.; Walker, D. G.; Valentine, J. G. Probing and Controlling Photothermal Heat Generation in Plasmonic Nanostructures. *Nano Lett.* **2013**, *13*, 1023-1028.

[8] Alabastri, A.; Malerba, M.; Calandrini, E.; Manjavacas, A.; De Angelis, F.; Toma, A.; Proietti Zaccaria, R. Controlling the Heat Dissipation in Temperature-Matched Plasmonic Nanostructures *Nano Lett* **2017**, *17*, 5472-5480.

[9] B. H.; Xu, X. F.; Wang, C. R. Active Gratings Tuned by Thermoplasmonics Induced Phase Transition in Vanadium Dioxide Thin Films . *Opt. Lett.* **2016**, *41*, 5768-5771.

[10] Cao, L.; Barsic, D. N.; Guichard, A. R.; Brongersma, M. L. Plasmon-Assisted Local Temperature Control to Pattern Individual Semiconductor Nanowires and Carbon Nanotubes. *Nano Lett*. **2007**, *7*, 3523-3527.

[11] DiMartino, G.; Michaelis, F. B.; Salmon, A. R.; Hofmann, S.; Baumberg, J. J.. Controlling Nanowire Growth by Light. *Nano Lett.* **2015,** *15*, 7452-7457.

[12] Alabastri, A.; Toma, A.; Malerba, M.; De Angelis, F.; Proietti Zaccaria, R., High Temperature Nanoplasmonics: The Key Role of Nonlinear Effects. *ACS Photonics* **2015,** *2* (1), 115-120.

[13] Hirsch, L. R.; Stafford, R. J.; Bankson, J. A.; Sershen, S. R.; Rivera, B.;Price, R. E.; Hazle, J. D.; Halas, N. J.; West, J. L. Nanoshell-mediated Near-infrared Thermal Therapy of Tumors under Magnetic Resonance Guidance . *Proc. Natl. Acad. Sci.* **2003**, *100*, 13549-13554.

[14] Baffou, G.; Berto, P.; Bermùdez Urena, E.; Quidant, R.; Monneret, S.;Polleux, J.; Rigneault, H. Photoinduced Heating of Nanoparticle Arrays. *ACS Nano* **2013**, *7*, 6478-6488.
[15] Mayerhöfer, T. G.; Knipper, R.; Hübner, U.; Cialla-May, D.; Weber, K.; Meyer, H.-G.; Popp, J. Ultra Sensing by Combining Extraordinary Optical Transmission with Perfect Absorption. *ACS Photonics* **2015**, *2*, 1567-1575.
[16] Cortés, E.; Xie, W.; Cambiasso, J.; Jermyn, A.; Sundararaman, R.; Narang, P.; Schlücker, S.; Maier, S. Plasmonic Hot Electron Transport Drives Nano-localized Chemistry. *Nat. Commun.* **2017**, *8*, 14880.
[17] Mukherjee, S.; Libisch, F.; Large, N.; Neumann, O.; Brown, L. V.; Cheng, J.; Lassiter, J. B.; Carter, E. A.; Nordlander, P.; Halas, N. J. Hot Electrons Do the Impossible: Plasmon-Induced Dissociation of H2 on Au. *Nano Lett.* **2013**, *13*, 240-247.
[18] Von Maltzahn, G.; Park, J. H.; Lin, K. Y.; Singh, N.; Schwöppe, C.; Mesters, R.; Berdel, W. E.; Ruoslahti, E.; Sailor, M. J.; Bhatia, S. N. Nanoparticles that Communicate In Vivo to Amplify Tumor Targeting. *Nat. Mater.* **2011,** *10*, 545–552.
[19] Crick, C. R.; Albella, P.; Kim, H.-J.; Ivanov, A. P.; Kim, K.-B.; Maier, S. A.; Edel, J. B. Low-Noise Plasmonic Nanopore Biosensors for Single Molecule Detection at Elevated Temperatures. *ACS Photonics* **2017**, *4*, 2835-2842.
[20] Rybka, T.; Ludwig, M.; F. Schmalz, M.; Knittel, V.; Brida, D.; Leitenstorfer, A. Sub-cycle Optical Phase Control of Nanotunnelling in the Single-electron Regime. *Nat. Photonics.* **2016**, *10*, 667-670.
[21] Lahiri, B.; Holland, G.; Aksyuk, V.; Centrone, A. Nanoscale Imaging of Plasmonic Hot Spots and Dark Modes with the Photothermal-Induced Resonance Technique. *Nano Lett.* **2013**, *13*, 3218-3224.
[22] Katzenmeyer, A. M.; Chae, J.; Kasica, R.; Holland, G.; Lahiri, B.; Centrone, A.; Nanoscale Imaging and Spectroscopy of Plasmonic Modes with the PTIR Technique. *Adv. Opt. Mater.* **2014**, *2*, 718–722.
[23] Aksyuk, V.; Lahiri, B.; Holland G.; Centrone, A. Near-field Asymmetries in Plasmonic Resonators. *Nanoscale* **2015**, *7*, 3634-3644.
[24] Chae, J.; Lahiri, B.; Centrone A. Engineering Near-Field SEIRA Enhancements in Plasmonic Resonators. *ACS Photonics*, **2016**, *3*, 87–95.
[25] Osawa, M.; Ikeda, M. Surface-Enhanced Infrared Absorption of p-Nitrobenzoic Acid Deposited on Silver Island Films: Contributions of Electromagnetic and Chemical Mechanisms. *J. Phys. Chem.* **1991**, *95*, 9914– 9919.
[26] Neubrech, F.; Huck, C.; Weber, K.; Pucci, A.; Giessen, H.; Surface-Enhanced Infrared Spectroscopy Using Resonant Nanoantennas. *Chem. Rev.* **2017**, *117* (7), 5110–5145.
[27] Maulini, R.; Mohan, A.; Giovannini, M.; Faist, J. External Cavity Quantum-cascade Laser Tunable from 8.2 to 10.4 μm Using a Gain Element with a Heterogeneous Cascade. *Appl. Phys. Lett.* **2006**, *88*, 201113.
[28] Dazzi, A.; Glotin, F.; Carminati, R. Theory of Infrared Nanospectroscopy by Photothermal Induced Resonance. *J. Appl. Phys.* **2010**, *107*, 124519.
[29] Felts, J. R.; Kjoller, K.; Lo, M.; Prater, C. B.; King, W. P. Nanometer-Scale Infrared Spectroscopy of Heterogeneous Polymer Nanostructures Fabricated by Tip-Based Nanofabrication. *ACS Nano* **2012**, *6*, 8015-8021.
[30] Lu, F.; Jin, M.; Belkin, M. A. Tip-enhanced Infrared Nanospectroscopy via Molecular Expansion Force Detection. *Nat. Photonics* **2014**, *8*, 307-312.
[31] Mertiri, A.; Altug, H.; Hong, M. K.; Mehta, P.; Mertz, J.; Ziegler, L. D.; Erramilli, S. Midinfrared Photothermal Spectroscopy Using Zharov Splitting and Quantum Cascade Lasers. *ACS Photonics* **2014**, *1*, 696-702.
[32] Khanikaev, A.; Arju, N.; Fan, Z.; Purtseladze, D.; Lu, F.; Lee, J.; Sarriugarte, P.; Schnell, M.; Hillenbrand, R.; Belkin, M.; Shvets, G. Experimental Demonstration of the Microscopic Origin of Circular Dichroism in Two-dimensional Metamaterials. *Nature Commun.* **2016**, *7*, 12045.
[33] Felts, J. R.; Law, S.; Roberts, C. M.; Podolskiy, V.; Wasserman, D. M.; King, W. P. Near-field Infrared Absorption of Plasmonic Semiconductor Microparticles Studied Using Atomic Force Microscope Infrared Spectroscopy**.** *Appl. Phys. Lett.* **2013**, *102*, 152110.
[34] Giannini, V.; Francescato, Y. Amrania, H.; Phillips, C. C.; Maier, S. A. Fano Resonances in Nanoscale Plasmonic Systems: A Parameter-Free Modeling Approach. *Nano Lett.* **2011**, *11*, 2835–2840.
[35] Wu, C.; Khanikaev, A. B.; Adato, R.; Arju, N.; Yanik, A. A.; Altug, H.; Shvets, G. Fano-resonant Asymmetric Metamaterials for Ultrasensitive Spectroscopy and Identification of Molecular Monolayers. *Nat. Materials* **2012**, *11*, 69–75.
[36] Limaj, O.; D'Apuzzo, F.; Di Gaspare, A.; Giliberti, V.; Domenici, F.; Sennato, S.; Bordi, F.; Lupi, S.; Ortolani, M. Mid-Infrared Surface Plasmon Polariton Sensors Resonant with the Vibrational Modes of Phospholipid Layers. *J. Phys. Chem. C* **2013**, *117*, 19119–19126.
[37] Huck, C.; Vogt, J.; Sendner, M.; Hengstler, D.; Neubrech, F.; Pucci, A. Plasmonic Enhancement of Infrared Vibrational Signals: Nanoslits versus Nanorods. *ACS Photonics* **2015**, *2*, 1489-1497.
[38] Neuman, T.; Huck, C.; Vogt, J.; Neubrech, F.; Hillenbrand, R.; Aizpurua, J.; Pucci, A. Importance of Plasmonic Scattering for an Optimal Enhancement of Vibrational Absorption in SEIRA with Linear Metallic Antennas. *J. Phys. Chem. C* **2015**, *119*, 26652-26662.
[39] Baldassarre, L.; Sakat, E.; Frigerio, J.; Samarelli, A.; Gallacher, K.; Calandrini, E.; Isella, G.; Paul, D. J.; Ortolani, M.; Biagioni, P. Midinfrared Plasmon-Enhanced Spectroscopy with Germanium Antennas on Silicon Substrates. *Nano Lett.* **2015**, 15, 7225–7231.

[40] Garoli, D.; Calandrini, E.; Bozzola, A.; Ortolani, M.; Cattarin, C.; Barison, S.; Toma, A.; De Angelis, F. Boosting Infrared Energy Transfer in 3D Nanoporous Gold Antennas. *Nanoscale* **2017**, *9*, 915-922.
[41] Schnell, M.; Garcia-Etxarri, A.; Huber, A.; Crozier, K.; Aizpurua, J.; Hillenbrand, R. Controlling the Near-field Oscillations of Loaded Plasmonic Nanoantennas. *Nat. Photonics* **2009**, *3*, 287-291.
[42] Rezus, Y.; Selig, O. Impact of Local-field Effects on the Plasmonic Enhancement of Vibrational Signals by Infrared Nanoantennas. *Opt. Express* **2016**, *24*, 12202-12227.
[43] De Angelis, F.; Malerba, M.; Patrini, M.; Miele, E.; Das, G.; Toma, A.; Zaccaria, R. P.; Di Fabrizio, E. 3D Hollow Nanostructures as Building Blocks for Multifunctional Plasmonics. *Nano Lett.* **2013**, *13*, 3553–3558.
[44] Rakic, A. D.; Djurisic, A. B. ; Elazar, J. M.; Majewski, M. L. Optical properties of metallic films for vertical-cavity optoelectronic devices. *Appl. Opt.* **1998,** *37*, 5271-5283.
[45] Malerba, M.; Alabastri, A.; Miele, E.; Zilio, P.; Patrini, M.; Bajoni, D.; Messina, G. C.; Dipalo, M.; Toma, A.; Zaccaria, R. P.; De Angelis, F. 3D Vertical Nanostructures for Enhanced Infrared Plasmonics. *Sci. Rep.* **2015**, *5*, 16436.
[46] Calandrini, E.; Venanzi, T.; Appugliese, F.; Badioli, M.; Giliberti, V.; Baldassarre, L.; Biagioni, P.; De Angelis, F.; Klesse, W. M.; Scappucci, G.; Ortolani, M. Mapping the Electromagnetic Field Confinement in the Gap of Germanium Nanoantennas with Plasma Wavelength of 4.5 micrometers. *Appl. Phys. Lett.* **2016**, *109*, 121104.
[47] Donner, J. S.; Thompson, S. A.; Kreuzer, M. P.; Baffou, G.; Quidant, R. Mapping Intracellular Temperature Using Green Fluorescent protein. *Nano Lett.* **2012**, *12*, 2107-2111.
[48] Coppens, Z. J.; Li, W.; Walker, D. G.; Valentine, J. G. Probing and Controlling Photothermal Heat Generation in Plasmonic Nanostructures. *Nano Lett.* **2013**, *13*, 1023-1028.
[49] Herzog, J. B.; Knight, M. W.; Natelson, D. Thermoplasmonics: Quantifying Plasmonic Heating in Single Nanowires. *Nano Lett.* **2014**, *14*, 499-503.
[50] Picardi, G.; Colas, F. J.; Gillibert, R.; de la Chapelle, M. L. Spectral Shift of the Plasmon Resonance Between the Optical Extinction and Absorption of Gold and Aluminum Nanodisks. *J. Phys. Chem. C* **2016**, *120*, 26025-26033.
[51] Chae, J.; An, S.; Ramer, G.; Stavila, V.; Holland, G.; Yoon, Y.; Talin, A. A.; Allendorf, M.; Aksyuk, V. A.; Centrone A. Nanophotonic Atomic Force Microscope Transducers Enable Chemical Composition and Thermal Conductivity Measurements at the Nanoscale. *Nano Lett.*, **2017**, *17*, 5587–5594.
[52] Alonso-González, P.; Albella, P.; Neubrech, F.; Huck, C.; Chen, J.; Golmar, F.; Casanova, F.; Hueso, L. E.; Pucci, A.; Aizpurua, J.; Hillenbrand, R. Experimental Verification of the Spectral Shift between Near- and Far-Field Peak Intensities of Plasmonic Infrared Nanoantennas. *Phys. Rev. Lett.* **2013**, *110*, 203902.
[53] Bigelow, N. W.; Masiello, D. J. Thermal Signatures of Plasmonic Fano Interferences: Toward the Achievement of Nanolocalized Temperature Manipulation. *J. Phys. Chem. Lett.* **2014**, *5*, 1347-1354.
[54] Schnell, M.; Garcia-Etxarri, A.; Alkorta, J.; Aizpurua, J.; Hillenbrand, R. Phase-Resolved Mapping of the Near-Field Vector and Polarization State in Nanoscale Antenna Gaps. *Nano Lett* **2010**, *10*, 3524-3528.
[55] Neubrech, F.; Pucci, A.; Cornelius, T. W.; Karim, S.; García-Etxarri, A.; Aizpurua, J. Resonant Plasmonic and Vibrational Coupling in a Tailored Nanoantenna for Infrared Detection. *Phys. Rev. Lett.* **2008**, *101*, 157403.
[56] Lu, F.; Belkin, M. A. Infrared Absorption Nano-spectroscopy Using Sample Photoexpansion Induced by Tunable Quantum Cascade Lasers. *Opt. Express* **2011**, *19*, 19942-19947.
[57] Baffou, G.; Quidant, R.; García de Abajo, F. J. Nanoscale Control of Optical Heating in Complex Plasmonic Systems. *ACS Nano* **2010**, *4*, 709-716.
[58] Giliberti, V.; Badioli, M.; Nucara, A.; Calvani, P.; Ritter, E.; Puskar, L.; Aziz, E. F.; Hegemann, P.; Schade, U.; Ortolani, M.; Baldassarre, L. Heterogeneity of the Transmembrane Protein Conformation in Purple Membranes Identified by Infrared Nanospectroscopy. *Small* **2017**, *13*, 1701181.
[59] Olynick, D. L.; Cord, B.; Schipotinin, A.; Ogletree, D. F.; Schuck P. J. Electron-beam Exposure Mechanisms in Hydrogen Silsesquioxane Investigated by Vibrational Spectroscopy and In Situ Electron-beam-induced Desorption. *J. Vac. Sci. Technol. B* **2010**, *28*, 581.
[60] Liu, X.; Starr, T.; Starr, A. F.; Padilla, W. J. Infrared Spatial and Frequency Selective Metamaterial with Near-Unity Absorbance. *Phys. Rev. Lett.* **2010**, *104*, 207403.
[61] Jiang, Z. H.; Yun, S.; Toor, M.; Werner, D. H.; Mayer, T. S. Conformal Dual-Band Near-Perfectly Absorbing Mid-Infrared Metamaterial Coating. *ACS Nano* **2011**, *5* (6), 4641–4647.

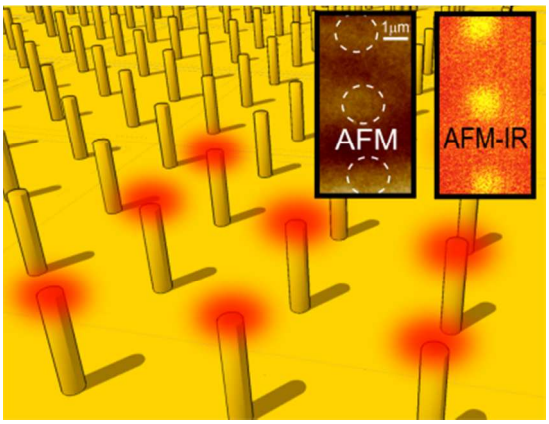

Table Of Contents Figure

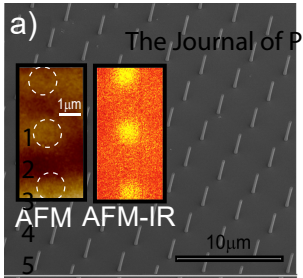

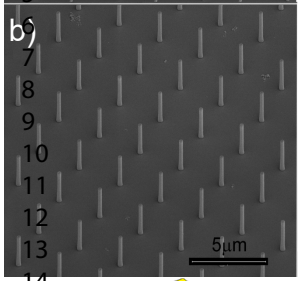

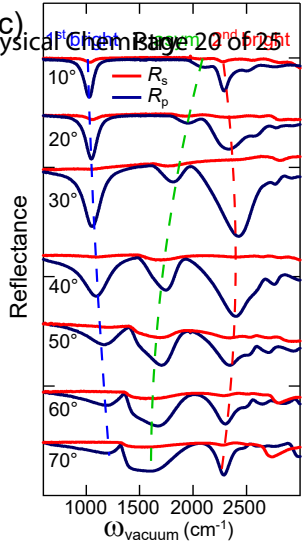

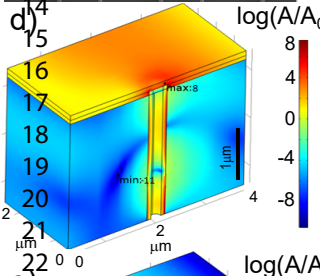

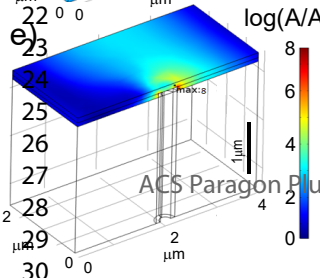

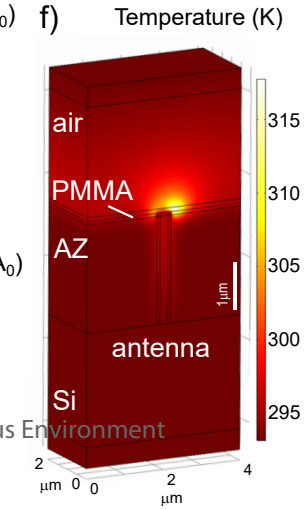

ACS Paragon Plus Environment

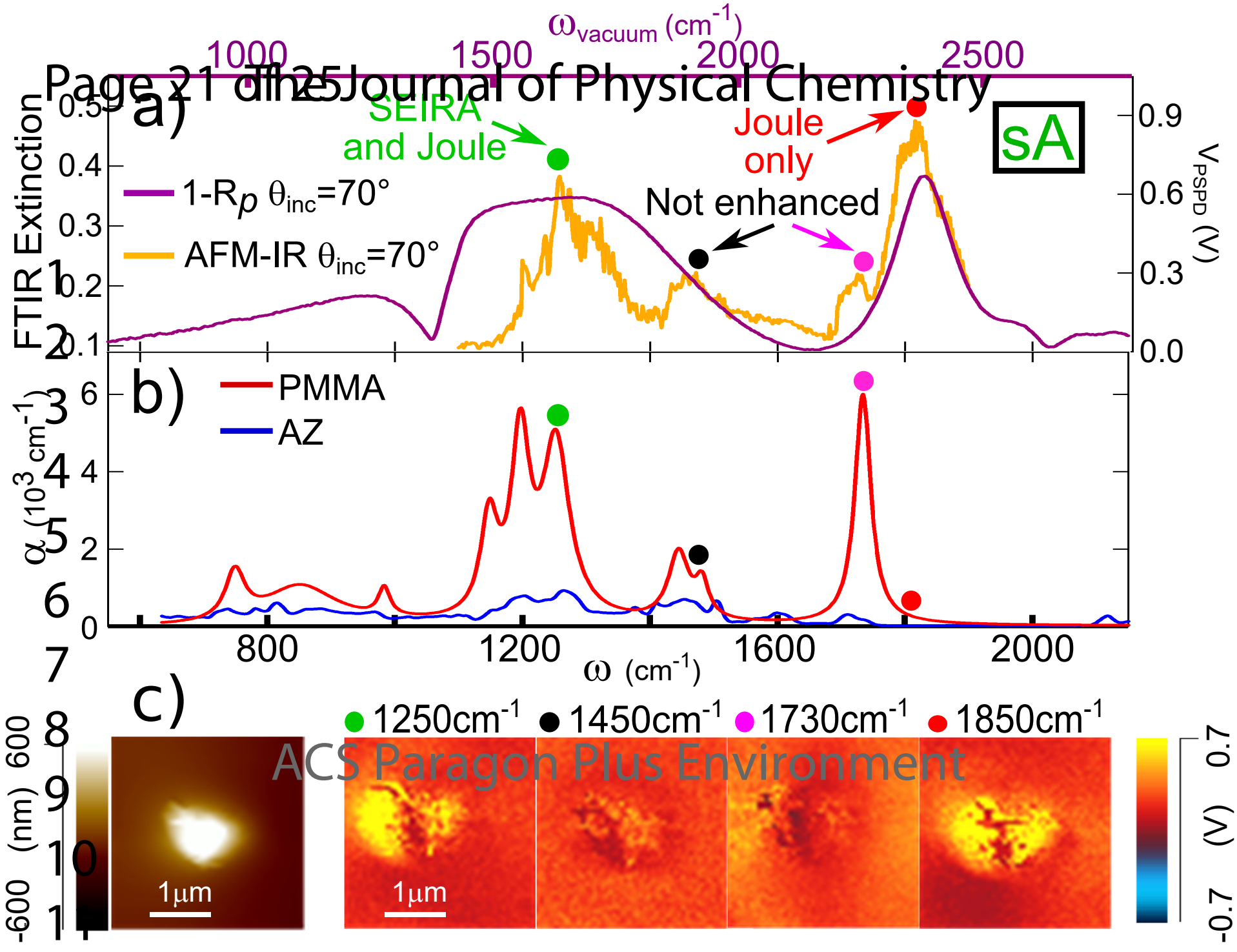

ACS Paragon Plus Environment

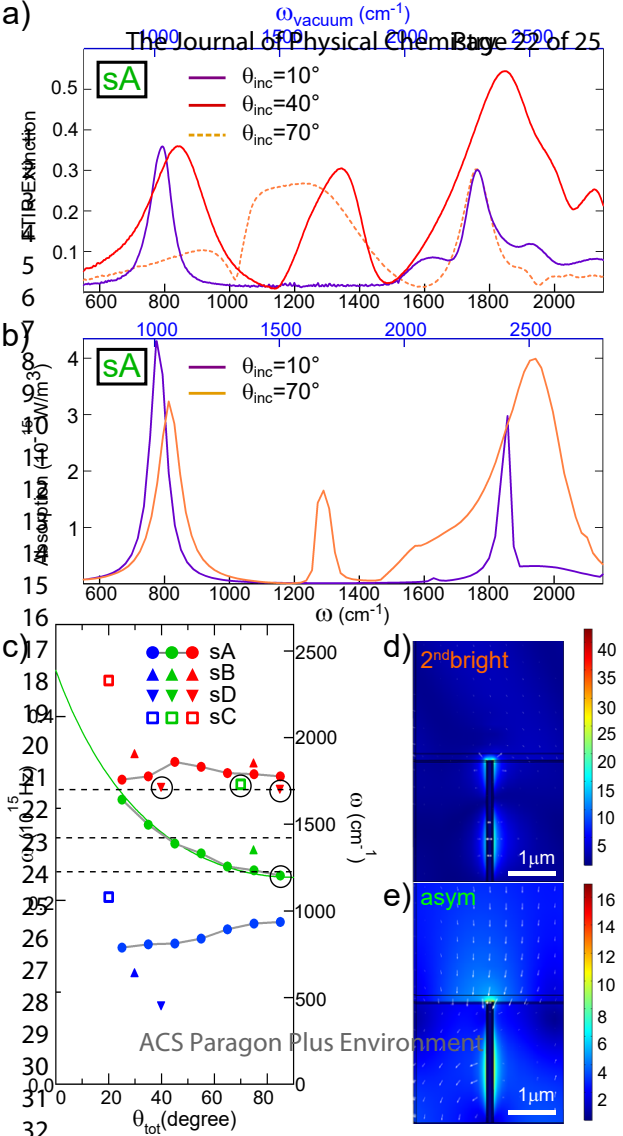

ACS Paragon Plus Environment

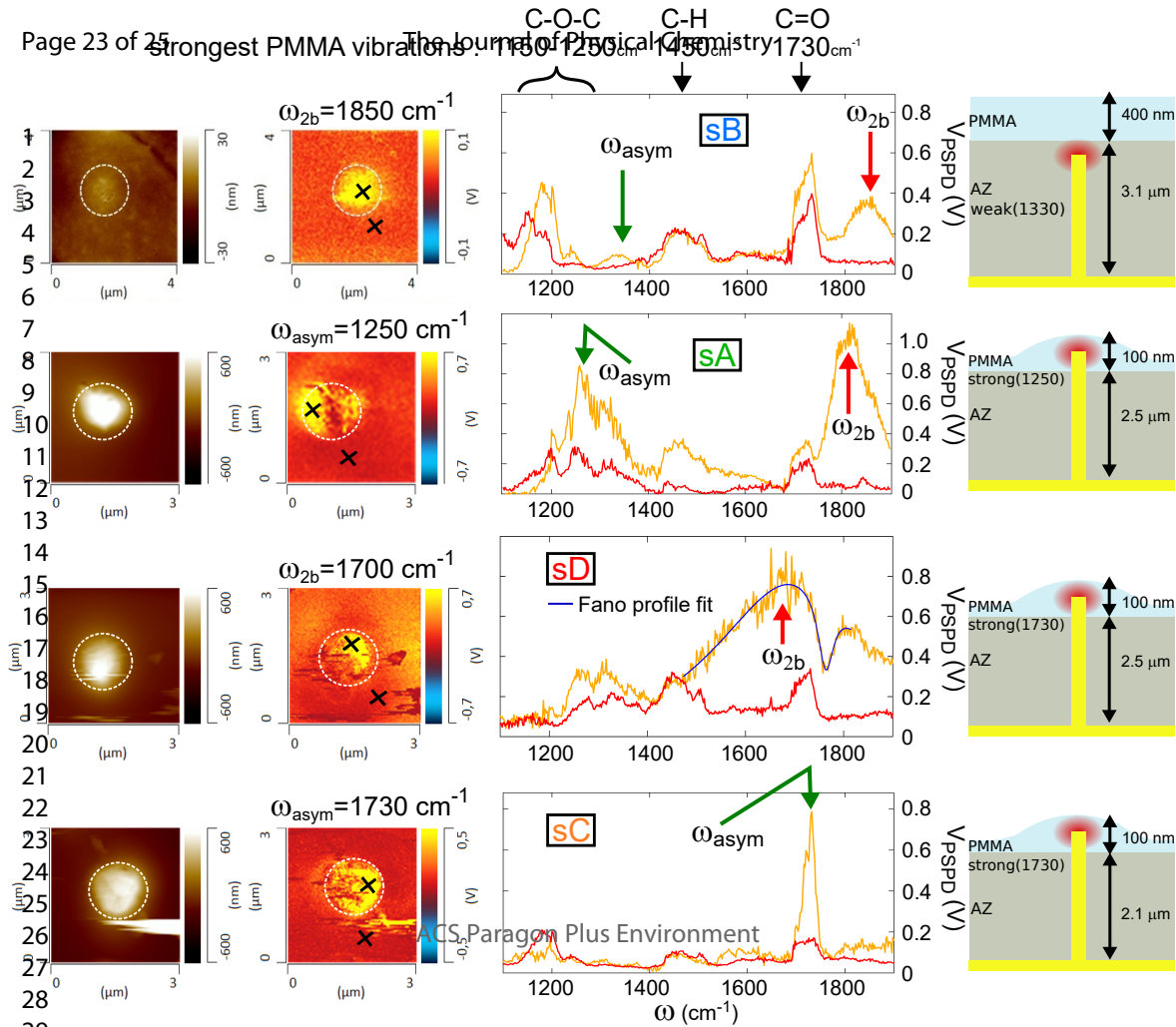
Strongest PMMA vibrations : 1150-1250cm-1
C-O-C
C-H 1450cm-1
C=O 1730cm-1
ω2b=1850 cm-1
ωasym=1250 cm-1
ω2b=1700 cm-1
ωasym=1730 cm-1
sB
sA
sD
sC
ωasym
ω2b
Fano profile fit
PMMA
AZ
weak(1330)
strong(1250)
strong(1730)
400 nm
100 nm
3.1 µm
2.5 µm
2.1 µm
VPSPD (V)
ω (cm-1)
ACS Paragon Plus Environment

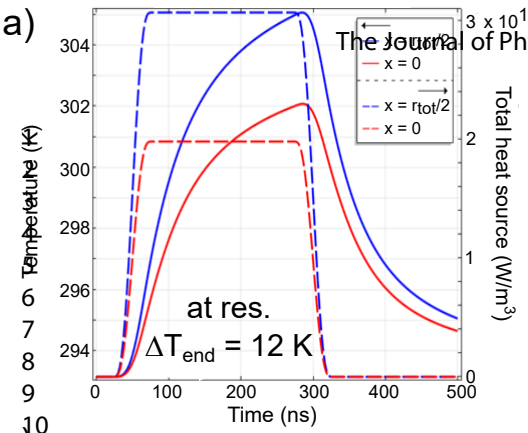

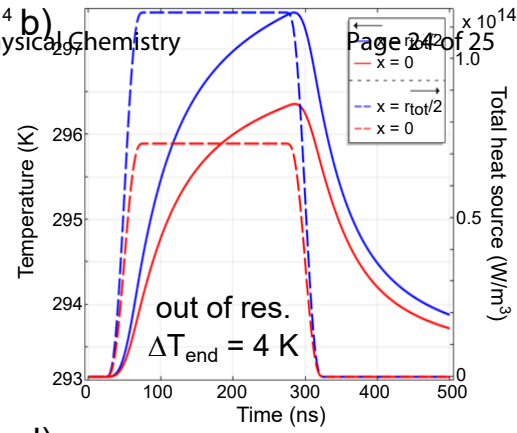

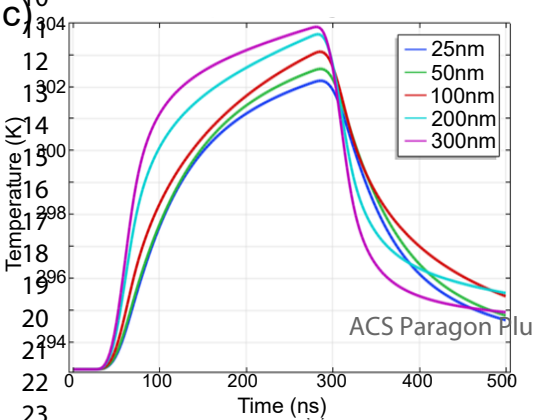

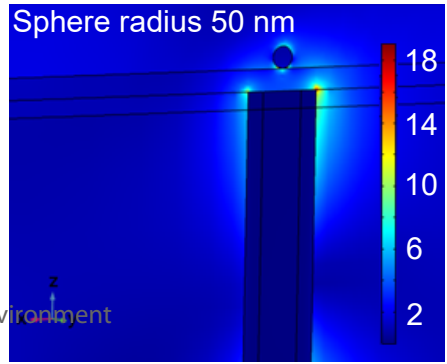

ACS Paragon Plus Environment

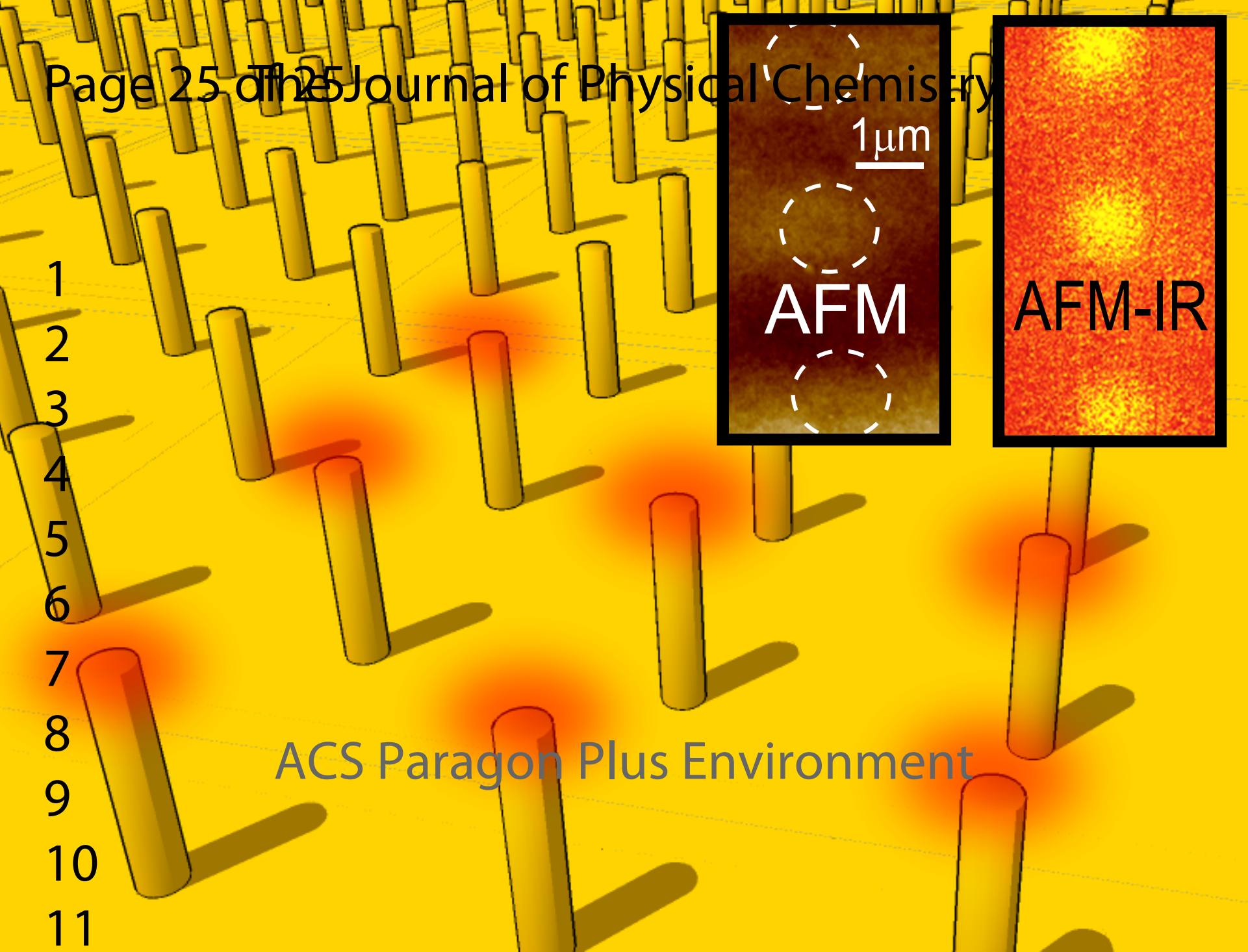
1μm
AFM
AFM-IR
ACS Paragon Plus Environment